



Precision additive manufacturing of NiTi shape memory parts using micro-laser powder bed fusion

Saeed Khademzadeh¹

Received: 28 April 2021 / Accepted: 7 November 2021 / Published online: 30 November 2021
© The Author(s), under exclusive licence to Springer Nature Switzerland AG 2021

Abstract

Nickel–titanium (NiTi) is a promising alloy for biomedical applications due to its unique combination of functional properties such as shape memory effect, superelasticity behavior and biocompatibility. In particular, additive manufacturing of complex NiTi parts containing micro features has received increased attention in bone tissue engineering. Micro-scale additive manufacturing using powder bed techniques such as laser powder bed fusion raises the need to develop new regimes of process parameters. In this research, micro-laser powder bed fusion (μ LPBF) was served to fabricate single-phase austenitic nickel-titanium dense and porous materials. The focus of the first part of this study was on the phase transformation behaviour of μ LPBF-built NiTi before and after various heat treatment cycles. Investigations revealed that post process age hardening heat treatment has a significant effect on phase transformation temperatures of μ LPBF-built NiTi. In the second part of this study, a new strategy was employed to decrease the deviation of NiTi lattice structures with respect to the predesigned models. Results showed that precision additive manufacturing of single-phase NiTi is feasible through applying different μ LPBF process parameters for border and hatching areas. With respect to nominal geometrical models, 13% and 24% deviations of pore diameter were calculated in NiTi lattice structures containing 580 μ m and 380 μ m pores, respectively.

Keywords Additive manufacturing · Micro-laser powder bed fusion · Shape memory alloys · Differential scanning calorimetry

List of symbols

E	Input energy density (J/mm^3)
P	Laser power (W)
V	Scanning speed (mm/s)
dh	Hatching distance (mm)
t	Layer thickness (mm)
Ra	Roughness (μm)
d	Laser spot diameter (mm)
r_0	Beam radius ($d/2$)
r	Radial position
E_{el}	Elastic modulus (GPa)
σ_y	Yield strength (MPa)
K	Thermal conductivity (W/cm K)
S	Standard error (μm)
D_n	Nominal pore diameter (μm)
D_a	As-built pore diameter (μm)
n	Number of measurements

1 Introduction

Equiatomic nickel–titanium (NiTi) alloy (known as Nitinol) exhibits unique properties such as the shape-memory effect (SME) and superelasticity (SE) [1, 2]. As a result of SE and SME behaviors, NiTi alloy can restore large strains up to 8% by heating and unloading, respectively [3]. Due to these unique properties and thanks to general characteristics such as low stiffness, biocompatibility, damping characteristics, and corrosion behavior, NiTi is a suitable candidate for biomedical applications (e.g., bone plates, bone screws, and stents) [4, 5]. Challenges associated with the manufacturing of this alloy using conventional methods such as casting, machining, or powder metallurgy have hindered the industrial application of NiTi especially when the complex shaped parts are needed. The processability challenges of NiTi can be attributed to many factors such as high reactivity, high strength and poor machinability of this alloy. Therefore, NiTi parts are limited to simple geometries such as bars and sheets [3, 6, 7]. According to the abovementioned points, near net shape manufacturing or reducing production steps are in priorities when appropriate manufacturing method

✉ Saeed Khademzadeh
saeed.khademzadeh@unipd.it

¹ Department of Industrial Engineering (DII), University of Padova, Via Venezia, 1, 35129 Padova, Italy

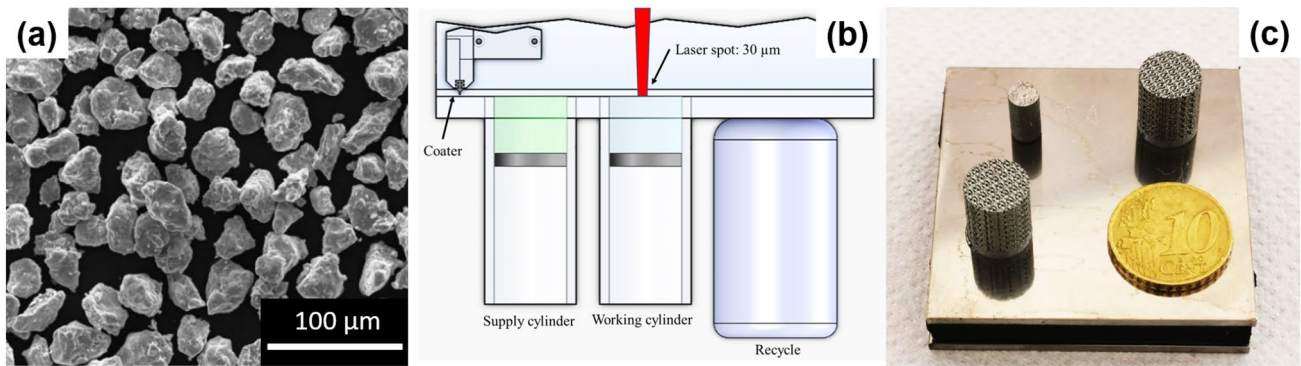


Fig. 1 **a** SEM micrograph of pre-alloyed $\text{Ni}_{50.8}\text{Ti}_{49.2}$ powder produced by EIGA process, **b** schematic of laser powder bed fusion machine (SISMA) developed for micro-fabrication, **c** μLPBF processed NiTi bulk and lattice samples

is going to be selected for fabrication of NiTi parts. In the past decade, Additive Manufacturing (AM) techniques have gained significant attention to overcome the manufacturing constraints associated with the fabrication of complex geometries and difficult-to-machine materials. Fabrication of lattice NiTi presents a combination of both manufacturing constraints i.e., complex geometries and difficult-to-machine materials. Moreover, NiTi is a multiphase alloy with a multistep austenite–martensite phase transformation which is the responsible for its unique shape memory behavior. Therefore, phase composition control during the production is another challenge that should be addressed. The presence of unwanted secondary phases and improper phase composition may result in deterioration of shape memory effect and super elasticity. Near net shape additive manufacturing of complex NiTi parts is essential to eliminate or minimize the postprocessing steps that would be difficult and cost consuming [8]. Among various metal AM techniques, laser powder bed fusion (LPBF) has shown a great capability to implement complex structures such as lattice parts containing micro features. According to the literature, the input energy densities used for LPBF processing of NiTi ranged between 50 and 120 J/mm^3 [3]. It is noteworthy to mention that various process configurations and different powders have been used by researchers. In this research, these two main challenges i.e., phase composition and near net shape additive manufacturing of Ni-rich NiTi alloy were addressed by development of micro-laser powder bed fusion (μLPBF) process. Three levels of laser power were identified to produce dense defect-free NiTi parts and complex lattice structures. Present work investigates phase transformation behavior of $\text{Ni}_{50.8}\text{Ti}_{49.2}$ produced by μLPBF before and after heat treatment. Moreover, image analysis allowed geometrical measurements with the aim to evaluate the capability of μLPBF process for precision manufacturing.

2 Experimental details

2.1 Materials

Gas atomised (EIGA¹) NiTi powder with particle size of 15–45 μm and Ni content of 50.8 at% from TLS Technik GmbH (Bitterfeld) was used as starting material. The powder particle size distribution was measured to be $D_{10} = 22 \mu\text{m}$, $D_{50} = 33 \mu\text{m}$ and $D_{90} = 44 \mu\text{m}$. The morphology of powder particles is shown in Fig. 1a by a scanning electron microscope (SEM) micrograph. As can be seen in Fig. 1a, the initial powder batch contained near spherical and irregular shape particles. Powder flowability is a crucial requirement for LPBF processes. Rheology of the NiTi powder batch was measured by FT4 Powder Rheometer (Freeman Technology) through dynamic testing to evaluate the flowability of the initial powder. This experiment revealed that the basic flowability energy (BFE) and specific energy (SE) of the NiTi powder were 508 mJ and 2.54 mJ/g, respectively. BFE and SE determines the resistance of the powder to flow, whilst the powder is in motion inside a confined and unconfined chamber, respectively. Same analysis on commercial stainless steel spherical powder produced by Renishaw company for LPBF showed 1300 mJ and 2.3 mJ/g for BFE and SE. Therefore, it can be concluded that gas atomized NiTi powder used in this research has acceptable flowability and spreadability to be used for LPBF technology. Impurity contents of initial NiTi powder used in this research were 0.005 wt% of carbon, 0.028 wt% of oxygen and 0.001 wt% of nitrogen. According to ASTM 2063-05 [9], acceptable impurity levels for medical use of NiTi are Oxygen < 0.05 wt% and Carbon < 0.05 wt%. Therefore, starting powder fulfilled the requirements of the ASTM standard for medical applications.

¹ Electrode Induction Gas Atomization.

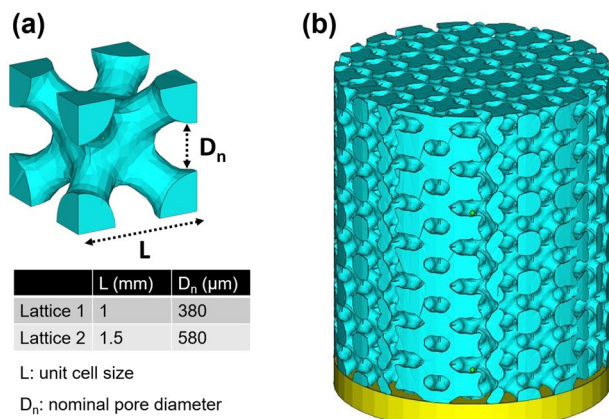


Fig. 2 **a** Diagonal unit cells in two dimensions, **b** designed lattice structure ($\varnothing = 10$ mm, $h = 11$ mm)

2.2 Micro-laser powder bed fusion process

Commercial LPBF system of type mysint100 (SISMA, Italy) was served to process dense NiTi cylindrical sample ($\varnothing = 4$ mm, $h = 10$ mm) and lattice structures ($\varnothing = 10$ mm, $h = 11$ mm). The configuration of LPBF system is schematically presented in Fig. 1b. This machine was equipped with an Ytterbium fiber laser (cw, $P_{\max, \text{theor}} = 200$ W, $\lambda = 1076.5$ nm). The beam profile was Gaussian, and the laser spot diameter was set at $30 \mu\text{m}$ to enhance the capability of the process for micro-fabrication. The μLPBF process of NiTi was carried out in an argon atmosphere with the oxygen level below 100 ppm to minimize unwanted chemical reactions. The layer thickness was selected according to the machine manufacturer's recommendation and based on the mean size of powder particles and kept constant to $25 \mu\text{m}$ in all experiments. Support generation and slicing of computer aided designed (CAD) models were done using software *Magics* (Materialise, SISMA). Thanks to multiphase support design in this research, the μLPBF -fabricated samples were cut from the titanium platform manually. Porous NiTi parts were designed by replicating of diagonal cubic unit cells (Fig. 2a). This unit cell was selected due to its strong geometrical isotropy and structural porosity (56%) close to trabecular bone. Unit cell size of 1 mm and 1.5 mm were selected which led to two pore diameters of $380 \mu\text{m}$ and $580 \mu\text{m}$, respectively. Cylindrical lattice with diameter of 10 mm and height of 11 mm was used in this study (Fig. 2b).

2.3 Attaining optimum process parameters

A comprehensive design of experiment was conducted to explore the optimum μLPBF process parameters with the aim to manufacture dense NiTi parts with appropriate phase compositions. The details are presented elsewhere [10]. An overview of used process parameters is presented in Table 1.

Table 1 μLPBF process parameters used for fabrication of NiTi

Parameter	Values
Power (P)	70–150
Scanning speed (V)	700–1100
Hatch distance (dH)	60, 100 μm
Layer thickness (t)	20, 25 μm
Energy densities (E)	50–120 J/mm^3
Laser spot diameter (dL)	30 μm
Oxygen level	< 200 ppm

The main objective in this step was set at finding optimized sets of process parameters in various levels of laser power and minimum input energy density.

2.4 Heat treatment

As-built cylindrical bulk samples were solid solutionized in the furnace (Carbolite Gero 30–3000 °C) at 1000 °C for 2 h (SS1) and 5 h (SS2) under argon atmosphere and then water quenched. Heat treatment temperatures were selected based on the binary Ni–Ti phase diagram. Subsequent age hardening was conducted at temperature of 300 °C for 1 h (Ag1) and 5 h (Ag2). Aged samples were water quenched at room temperature right after aging. An overview of four heat treatment cycles is presented in Table 2.

2.5 Characterizations

A small piece (15–40 mg) of as-built and heat-treated samples was used for Differential Scanning Calorimetry (DSC) using a *TA instruments DSC Q100* with $10 \text{ }^\circ\text{C}/\text{min}$ in nitrogen atmosphere to determine the transformation temperatures (TTs). All samples were polished prior to DSC analysis to ensure good thermal contact. The weight of sample was measured, and the sample was placed into an aluminum holding pan. An empty pan was used as a reference. The sample was then thermally cycled in a temperature range from -100 to $100 \text{ }^\circ\text{C}$ and the heat difference was recorded and plotted as a function of temperature. TTs were extracted from heat-temperature graphs using maximum gradient lines of transformation peaks. Scanning electron microscope (SEM) (Quanta 450) was used to reveal the surface topography of lattice structures. Image analysis was applied on SEM micrographs using software *Image J* to quantitatively evaluate the lattice structures in terms of accuracy of micro pores. Standard error of the estimate (S) was calculated for four individual pores in each lattice according to Eq. (1) [11]. For each pore, six diameter measurements were considered for calculation of deviation.

Table 2 Heat treatment cycles performed on NiTi bulk samples produced by μ LPBF

Heat treatment	Type	Temperature (°C)	Heating rate (°C/min)	Dwell time (h)	Quench
SS1	Solution annealing	1000	10	2	Water
SS2	Solution annealing	1000	10	5	Water
Ag1	Aging	300	10	1	Water
Ag2	Aging	300	10	5	Water

Table 3 LPBF process parameters used in the literature for fabrication of dense NiTi

	P (W)	V (mm/s)	t (mm)	dh (mm)	E (J/mm ³)	d (mm)	ρ (%)
Dadbakhsh et al. [14]							
HP	250	1100	0.03	0.06	126	0.08	99
LP	40	160		0.075	111		
Saedi et al. [15]	250	1250		0.12	55		
Shishkovsky et al. [16]							
HP	50	100	0.03	0.1	83	0.06	97
LP		160			52		

$$S = \sqrt{\frac{\sum_{i=0}^n (D_n - D_{ai})^2}{n-1}} \quad (1)$$

Compression tests were conducted using a universal testing machine (Quasar 25, Galdabini s.r.l., Italy). A crosshead speed of 0.2 mm/min was employed during loading while unloading was performed under force control at a rate of 100 N/s.

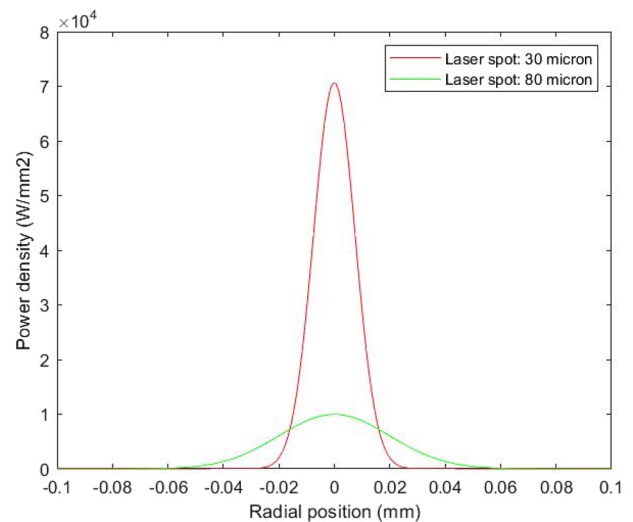
3 Results and discussion

3.1 Optimization of process parameters

Manipulation of input energy density in LPBF process is possible through the main process parameters as presented in the following equation [12]:

$$E = \frac{P}{V \cdot dh \cdot t} \quad (2)$$

A narrow window of optimum process parameters has been proposed by researchers for fabrication of dense and defect-free NiTi parts [9]. Table 3 summarizes the main LPBF process parameters used by three research teams aiming at relative bulk density higher than 99%. To the best of our knowledge, the minimum laser spot diameter of 80 μ m has been utilized for LPBF of NiTi. In this research, laser spot diameter of 30 μ m was selected to develop LPBF for microfabrication. Laser beams with Gaussian irradiance have symmetric distribution of intensity around the center of the beam that decreases as the distance from the center

**Fig. 3** Gaussian distribution of laser density as a function of radial distance at two different spot sizes of 30 μ m and 80 μ m

of the beam. The intensity of a Gaussian laser beam can be calculated using the following equation [13]:

$$I(r) = I_0 \exp\left(\frac{-2r^2}{r_0^2}\right) = \frac{2P}{\pi r_0^2} \exp\left(\frac{-2r^2}{r_0^2}\right) \quad (3)$$

The beam radius is defined as the radial distance at which the intensity of the beam reduces to $1/e^2$ the peak intensity. This area has about 87.5% of the total beam energy. At a constant laser power, the intensity distributions of two Gaussian laser beams with 30 μ m and 80 μ m laser spot diameter are presented in Fig. 3. A significant increase in intensity of peak by reducing the laser spot diameter from 80 to

Table 4 μ LPBF processing parameters developed for processing of NiTi

Set	Powder	P (W)	V (mm/s)	E (J/mm ³)	d (mm)	ρ (%)
LP	Ni _{50.8} Ti _{49.2} (15–45 μ m)	49	700	46	0.03	99
MP		70	1100	42		99.3
HP		150	1100	54		99.5

30 μ m is highlighted in Fig. 3. This notable difference in characteristics of laser may suggest new regimes of process parameters for fabrication of NiTi using 30 μ m spot laser diameter. Based on a comprehensive design of experiments, three different levels of process parameters based on laser power were obtained for fabrication of defect-free and dense austenitic NiTi material (Table 4).

Table 4 represents that increasing laser power enhanced the relative density of NiTi parts. MP and LP led to the relative density above 99%. Haberland et al. [2] reported that high input energy density results in impurity pick-up during the LPBF process. Low level of impurities is a key parameter for medical applications, which is the largest market for NiTi products [17]. To have an acceptable level of impurity according to ASTM F2063-05 [9], LP and MP sets of process parameters with input energy densities below 50 J/mm³ were used for fabrication of dense and lattice NiTi parts. It is notable to mention that both LP and MP set of parameters use same hatching distance of 0.6 mm which is an important parameter in definition of scanning strategy and will be discussed in the following. Using similar NiTi powder, Dadbakhsh et al. reported approximately 99% relative density for the samples produced by both low and high input energy densities (111 J/mm³ and E_{HP} = 126 J/mm³) [14]. It should be mentioned that all three sets of process parameters (LP, MP, and HP) were selected among a series of visually healthy parts that were manufactured in a small range of input energy densities. It seems that when the selection of process parameters is in an appropriate range of input energy density, the laser power is the most determinant factor in relative density of final products. Elahinia et al. [3] showed that high level of input energy density beyond a threshold level (74 J/mm³) reduces the density of NiTi parts due to the instability of melt pool and consequently pore formation between the adjacent tracks.

3.2 Phase transformation responses of as-built μ LPBF-NiTi

It is well understood that LPBF processing of NiTi may result in inhomogeneous microstructure and formation of secondary phases [9]. XRD analysis showed that all three sets of μ LPBF process parameters in current research led to formation of single phase austenitic NiTi [10]. It should be noted that XRD analysis has limitation in identification of small quantity of secondary phases. Therefore, complete

elimination of unwanted secondary phases in as fabricated samples is hardly possible. A reversible martensitic transformation of a low temperature phase (martensite with monoclinic B19 structure) to a high temperature phase (austenite with cubic B2 structure) is responsible for the shape memory effect and superelasticity of NiTi alloy. The B19 martensite can be obtained either by a single step transformation of B2 \rightarrow B19, or by a two-step transformation of B2 \rightarrow R-phase (intermediate phase) \rightarrow B19. The phase transformation temperatures are identified as M_s , M_f , A_s and A_f correspond to martensite start, martensite finish, austenite start and austenite finish temperatures, respectively. As presented in Fig. 4, DSC curve of initial prealloyed NiTi powder showed several peaks (multistage transformations). Based on DSC curve, B2 austenite is the predominant phase in the initial powder at room temperature since M_s is lower than room temperature (see Fig. 4). Multistage phase transformation of powder particles prior to μ LPBF process can be attributed to the inhomogeneity in chemical composition of powder particles [3]. Figure 4 depicts that after μ LPBF process of NiTi using both LP and MP parameters, single-stage phase transformations were identified in both heating (martensite \rightarrow austenite) and cooling (austenite \rightarrow martensite). The TTs are extracted from DSC curves and summarized in Table 5. LP and MP have the same hatching distance and very close input energy densities. As presented in Table 5, sample produced by MP set of process parameters with high laser power adjusted to high scanning speed showed lower TTs than LP sample. It has been previously reported that increasing input energy density in LPBF process leads to an increase in phase transformation temperatures [2]. In fact, high input energy density, which in this case comes from the low scanning speed or high laser power, raises the melt pool temperature. Since nickel has lower evaporation temperatures than titanium, the matrix composition shifts to higher titanium content after LPBF process due to evaporation of nickel. Slightly increase of input energy density from 42 J/mm³ in MP sample to 46 J/mm³ in LP sample, raised transformation temperatures which confirms the direct impact of input energy density on phase transformation temperatures rather than other process parameters such as laser power and scanning speed.

As presented in Fig. 4 and Table 5, low input energy density of LP and MP parameters led to martensite start temperatures fairly below room temperatures (M_s (LP): 5.4 $^{\circ}$ C and M_s (LP): -4.9 $^{\circ}$ C). Single step phase transformation from B2 austenite to B19' martensite at temperatures lower

Fig. 4 DSC responses of $\text{Ni}_{50.8}\text{Ti}_{49.2}$ initial powder and μLPBF processed NiTi by LP and MP parameters; showing the presence of austenite phase before and after the process at room temperature

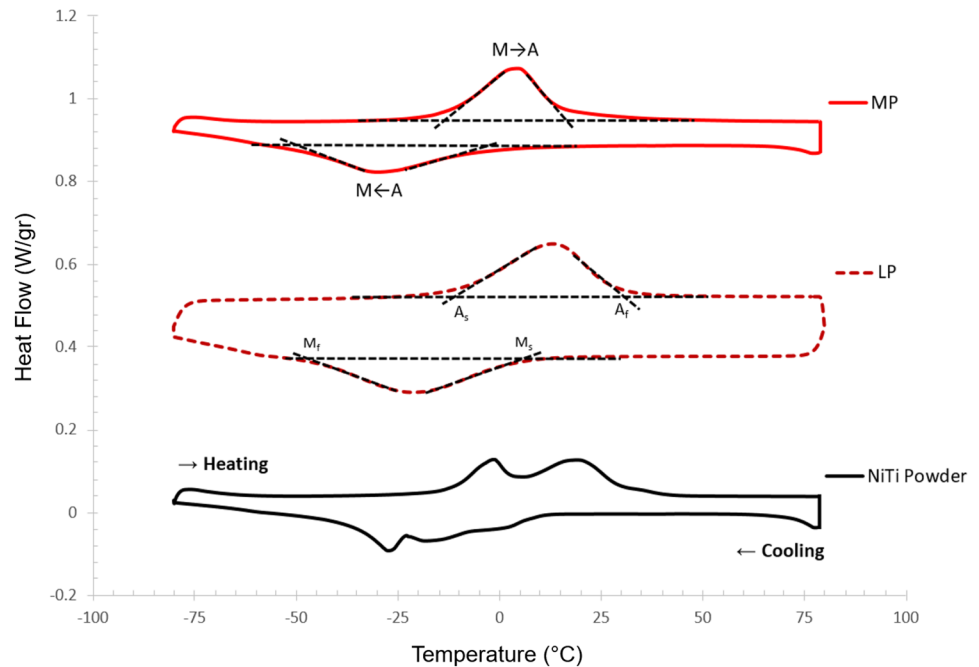


Table 5 TTs of μLPBF processed NiTi using LP and MP parameters

Set of process parameters	E (J/mm^3)	A_s ($^{\circ}\text{C}$)	A_f ($^{\circ}\text{C}$)	M_s ($^{\circ}\text{C}$)	M_f ($^{\circ}\text{C}$)
LP	46.66	-9.7	30.3	5.4	-46.5
MP	42.42	-14.3	16.8	-4.9	-50.1

A_s Austenite start temperature, A_f Austenite finish temperature, M_s Martensite start temperature, M_f Martensite finish temperature

than room temperature confirms that the majority volume fraction of both LP and MP samples are B2 austenite phase. This finding is in agreement with phase identification results previously reported by others. Dadbakhsh et al. [4] reported fully austenitic microstructures after LPBF process of NiTi using high input energy density ($P=250$ W, $V=1100$ mm/s, $E=120$ J/mm^3). They concluded that decrease in laser power and laser input energy density to 40 W and 111 J/mm^3 , respectively, led to significant increase in phase transformation temperatures and consequently mainly martensitic structure in as-built products. Shayesteh Moghaddam et al. [18] reported a multistep martensitic transformation in LPBF NiTi as-built samples using laser spot diameter of 80 μm . They reported that decrease in hatching distance improves the superelastic response as a result of homogenous microstructure. Single step austenite–martensite and martensite–austenite phase transformations in our study can be attributed to homogenous microstructure as a result of small spot laser diameter (30 μm) and small hatching distance (60 μm). Sharper austenite and martensite transformation peaks in MP sample suggest more homogenous

microstructure in MP sample compared to LP sample due to its higher laser power. Guan et al. [19] found that hatching space has the most significant influence on the microstructure and texture of the alloy produced by LPBF since it directly controls the remelting of adjacent tracks. Ma et al. [20] carried out simulations to capture the complex thermal history of the deposited material to predict the precipitation behavior of the Ni_4Ti_3 precipitates. They showed that precipitates would be most probable to form at small hatch distances and high input energy densities.

3.3 Multiphase support structures

Various lattice geometries have been developed to serve as support structures in LPBF with the aim to decrease the part deflection and act as a thermal heat sink. However, support removal is still one of the big issues associated with LPBF process. Additive manufacturing of metallic multiphase materials brings up this possibility to develop support structures with different phase composition in respect to the printed part. Same chemical composition, similar physical properties and different mechanical properties of LPBF part and support structure can create mechanically weak points at part–support interface preserving the main functions of support structures. In this research and using austenite–martensite phase transformation behavior of NiTi alloy, different phase compositions were proposed for printed part and support structures. The μLPBF process parameters used for part and support structures are presented in Table 6.

DSC curves of NiTi sample produced by MP set of parameters and support structure are presented in Fig. 5a.

Table 6 μ LPBF processing parameters used for support removal design

Set of process parameters	P (W)	V (mm/s)	E (J/mm ³)
LP	49	700	46.66
MP	70	1100	42.42
Support	49	437	74.75

As can be seen in this graph, specific process parameters with high input energy density increased the martensite start transformation temperature beyond the room temperature. It means that austenite–martensite transformation started during the cooling stage at 33.4 °C. Transformation temperatures of MP processed NiTi sample and support structure are extracted from Fig. 5 and summarized in Table 7. It can be seen that martensite finish temperature of support structure (− 15.9 °C) is lower than room temperature (25 °C) and suggests a mixed austenite–martensite microstructure in support structure after the process. It should be reminded that M_s and M_f of produced part using MP parameters are fairly below the room temperature (see Table 5).

Thermal conductivity, elastic modulus, and yield stress of martensitic and austenitic NiTi are presented in Table 8. Significant difference between yield strength and elastic modulus of austenitic and martensitic NiTi facilitates support removal after the process (see Fig. 5b).

3.4 Phase transformation responses of heat treated NiTi processed by μ LPBF

Post-process heat treatment of LPBF-NiTi through solution annealing and aging leads to enhancement in superelasticity of NiTi due to precipitation formation [23–25]. Elahinia et al. [3] showed that Ni_4Ti_3 precipitates with small relative distance could result in a perfect superelasticity. Precipitations can act as inhibitor for slipping within the crystal structure of B2 austenite NiTi and minimizes the plastic deformation. This phenomenon improves the superelasticity since the critical stress for stress induced martensite transformation is fairly lower than stress required for activation of slip system. Two different solution annealing and aging treatments were applied on bulk NiTi samples produced by μ LPBF (Table 2). Figure 6 shows the DSC responses of solid solutionized μ LPBF NiTi after heat treatment at 1000 °C for 2 h (SS1) and 5 h (SS2) in comparison with as-built MP sample. It is evident that after 2 h solutionizing of MP sample followed by water quenching (SS1), transformation peaks (austenite to martensite and martensite to austenite) became broaden. Sharp peaks after SS2 can be attributed to the dissolving of very fine secondary phases (that usually are formed during LPBF of NiTi) and consequently homogenous

microstructure. Moreover, from Fig. 6, it can be derived that TTs after both SS1 and SS2 decreased significantly. From Fig. 6, it can be concluded that 2 h solution annealing was not sufficient to obtain a homogenous microstructure since diffusion of Ni atoms is a time-dependent phenomenon.

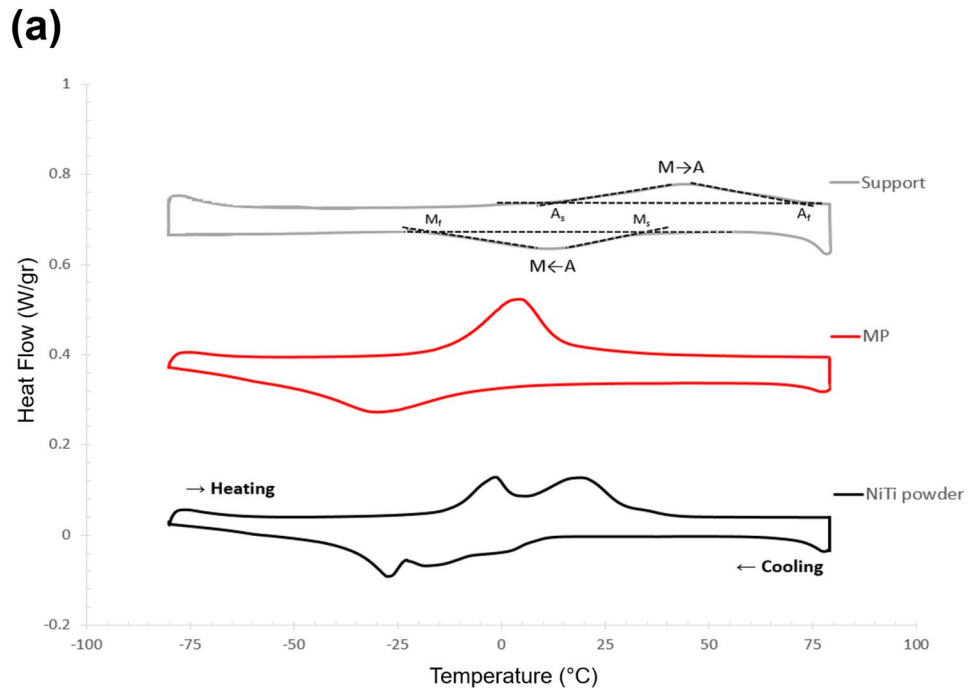
Figure 7 shows DSC responses of NiTi MP sample after solution annealing (SS2) and subsequent age hardening at 350 °C for 1 h (Ag1) and 5 h (Ag2). TTs are extracted from Fig. 7 and are presented in Table 9. It is clearly visible that aging heat treatment resulted in higher TTs and TTs increased with aging time that can be attributed to the formation of Ni-rich precipitates. Formation of Ni-rich precipitates depletes the Ni content of the matrix and increased TTs. As can be seen in Fig. 7, double-peak transformation appears during heating of aged samples. The first peak is related to martensite-R-phase transformation and the second peaks is related to R-phase-austenite phase transformation. Formation of intermediate R-phase after precipitating of Ni-rich second phases has been reported by other researchers [26–28]. Broad and multistep phase transformation after age hardening at 350 °C for 1 h (Ag1) can be attributed to the presence of ultra-fine coherent precipitates that can hinder the super elasticity effect. After aging of MP sample using Ag2 procedure and due to more aging time, the transformation peaks are quite sharp and distinct. On the contrary, the reverse transformation from austenite to martensite was done through a single distinct peak. Increase of aging time leads to increase the size of the precipitates and consequently results in higher strength of NiTi alloy [29]. It can be concluded that by controlling the age hardening heat treatment, superelasticity is achievable at both room temperature and body temperature.

3.5 Stress–strain responses

As-printed LP, MP samples are mostly austenitic at room temperature due to their low M_s temperature as presented in Table 6. It is hard to achieve superelasticity in as-built LPBF NiTi material [29]. Solutionized and age hardened LP and MP samples were compressed at 10 °C above A_f and the results are presented in Fig. 8. All the samples were loaded up to 950 MPa before reaching the critical stress for plastic deformation and then unloaded. The plateau during loading corresponds to stress-induced martensitic transformation. As can be seen in Fig. 8a, b, 15% and 12% deformation were occurred in solutionized LP and MP samples, respectively. More deformation in solutionized LP sample in comparison with solutionized MP sample can be explained by slightly higher input energy used for fabrication of LP sample which might have been led to the Ni loss and increase of ductility.

From Fig. 8, it can be seen that solutionized samples did not exhibit superelasticity which can be attributed to the low strength as a result of insufficient precipitation of Ni-rich

Fig. 5 a DSC responses of Ni_{5.8}Ti_{49.2} initial powder, NiTi sample produced by MP set of process parameters and support structure produced by specific process parameters presented in Table 6, **b** multiphase support design



(b)

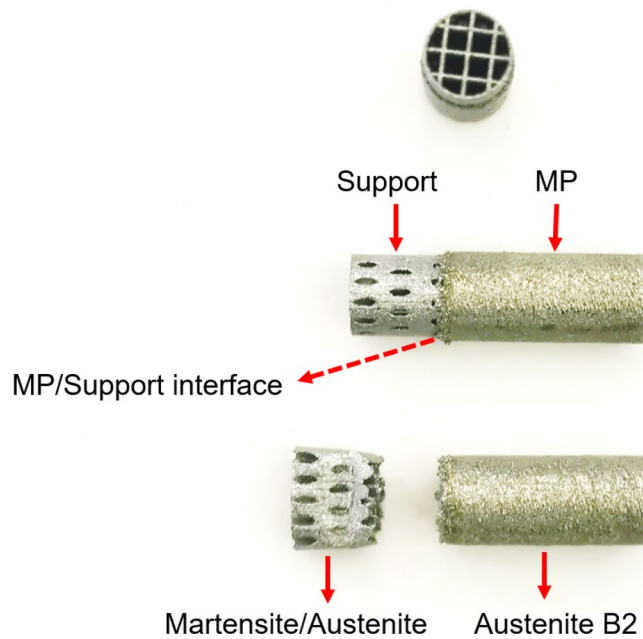


Table 7 TTs of NiTi MP sample and support structure

Set of process parameters	E (J/mm ³)	A_s (°C)	A_f (°C)	M_s (°C)	M_f (°C)
MP	42.42	-14.3	16.8	-4.9	-50.1
Support	74.75	13.5	73.1	33.4	-15.9

A_s Austenite start temperature, A_f Austenite finish temperature, M_s Martensite start temperature, M_f Martensite finish temperature

Table 8 Physical and mechanical properties of austenitic and martensitic NiTi

	K (W/cm K) [21]	E_{el} (GPa) [22]	σ_y (MPa) [22]
Austenitic NiTi	0.28	83	195–690
Martensitic NiTi	0.14	28–41	70–140

Fig. 6 DSC responses of NiTi MP sample before and after solid solution annealing at 1000 °C for 2 h (SS1) and 5 h (SS2)

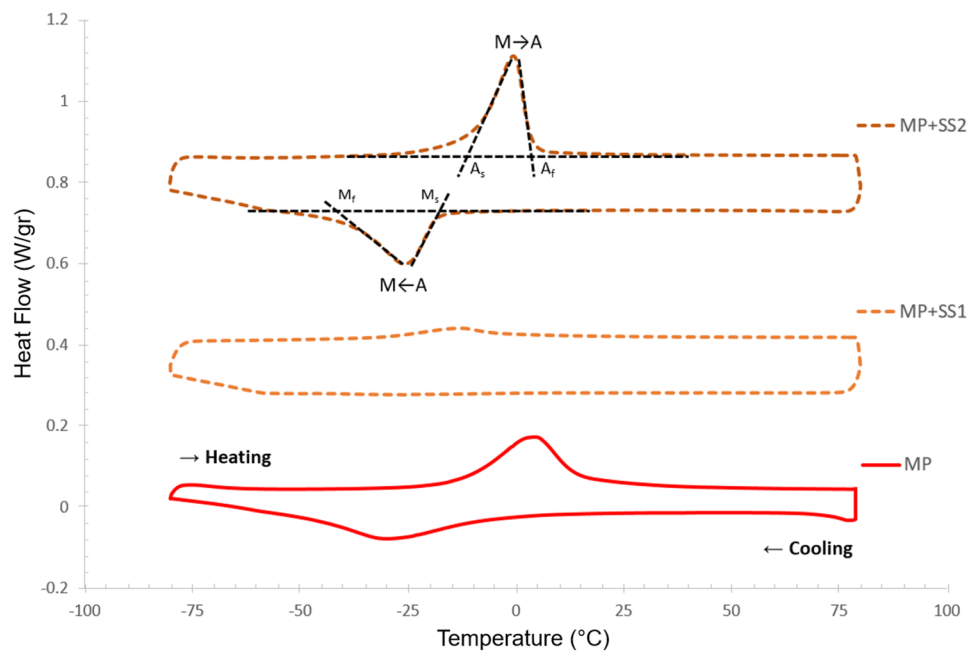


Fig. 7 DSC responses of NiTi MP as-built sample, after solid solution annealing at 1000 °C for 5 h (SS2) and after age hardening at 350 °C for 1 h (Ag1) and 5 h (Ag2)

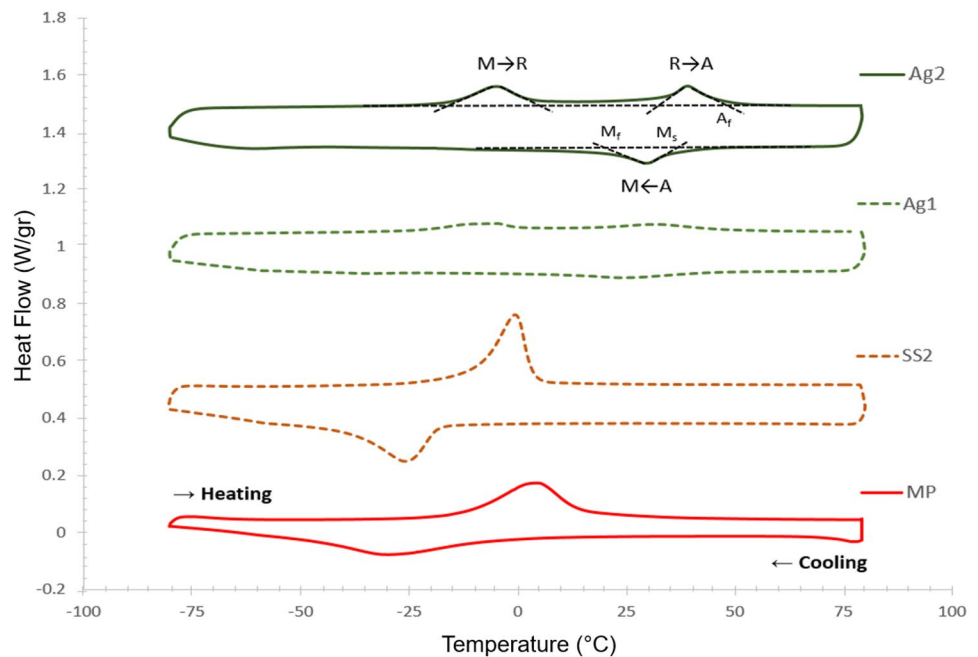


Table 9 TTs of NiTi MP sample before and after heat treatment

Heat treatment	A_s	A_f	M_s	M_f
As-built (MP)	-14.3	16.8	-4.9	-50.1
MP+SS2	-12.17	3.3	-18.63	-40.95
MP+SS2+Ag2	-	46.8	36.2	20.7

phases such as Ni_4Ti_3 . It is noteworthy to mention that less ductility (around 10%) has been reported in the literature for solutionized LPBF NiTi samples with similar chemical composition. It can be attributed to the homogenous microstructure as a result of small spot laser diameter and small hatching distance used in μ LPBF comparing to standard LPBF [18]. Superelasticity behavior can be observed in Ni-rich NiTi with coherent Ni_4Ti_3 precipitates. These precipitates increase the strength of austenite matrix and improve the superelasticity response of NiTi. Solid solution

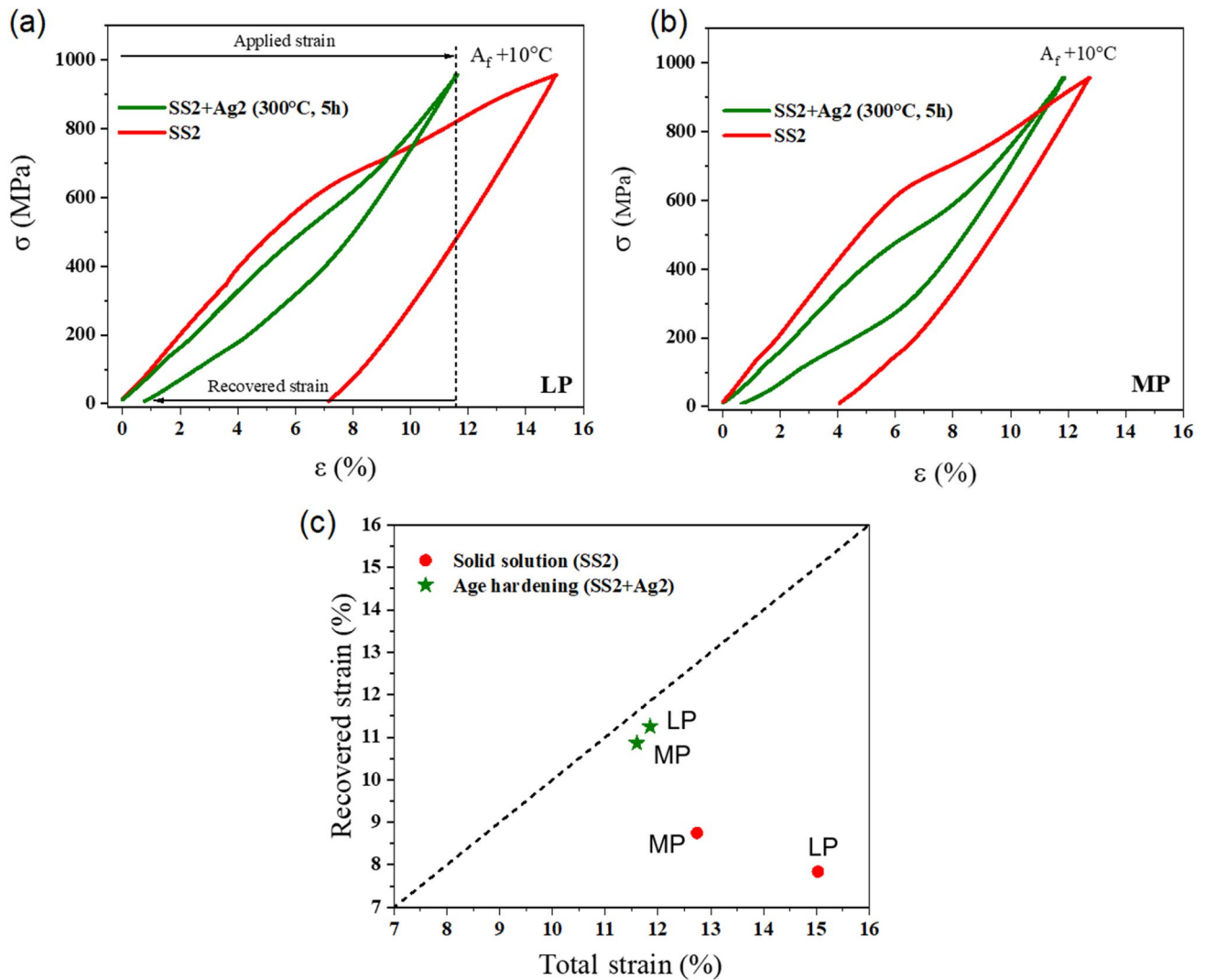


Fig. 8 Superelastic responses of solid solutionized and age hardened NiTi samples produced by LP and MP parameters at 10°C above A_f

and subsequent age hardening leads to the formation of Ni-rich precipitates [29, 30]. Precipitation hardening in aged samples increases the critical stress for plastic deformation compared to solutionized samples.

As presented in Fig. 8, both LP and MP samples aged at 350°C for 5 h showed almost perfect superelastic recovery. Irrecoverable strains for aged LP and MP samples were measured to be 0.6% and 0.56%, respectively. Recoverable strains of 7.84% and 8.75% were achieved for aged LP and MP samples, respectively. Saedi et al. [31] observed strain recovery of 5.5% with recovery ratio of 95% after solution annealing at 950°C for 5.5 h and aging at 350°C for 18 h on LPBF $\text{Ni}_{50.8}\text{Ti}_{49.2}$ (at. %).

Improved superelasticity in NiTi samples produced by μ LPBF in comparison with LPBF can be ascribed to the homogenous microstructure and precipitation characteristics. Small and coherent Ni-rich precipitates can increase

the strength of NiTi which improves the superelasticity. Small spot laser diameter used in μ LPBF might have been resulted in homogenous microstructure and consequently small and coherent precipitates that are evenly distributed in LPBF products. Figure 8c summarizes these tests showing the recovered strain as a function of total strain. It can be seen that the superelastic behavior of both LP and MP samples are similar after solution annealing and subsequent age hardening.

3.6 Geometrical accuracy of NiTi parts produced by μ LPBF

Metallic porous scaffolds are used to design implant prostheses thanks to their low elastic modulus that can be adjusted to be close to the human bone. Superelastic effect in NiTi alloy together with freeform manufacturing of LPBF brings

up a very promising combination for production of lattice structures. Geometrical accuracy is of great importance in production of complex lattice structures containing small features such as micro-pores. For instance, Li et al. [32] reported better cell adhesion and proliferation in titanium lattice structures with smaller pore size (300–400 μm) than structures with bigger pores (400–500 μm and 500–700 μm). LPBF process introduces process-induced geometrical defects that mainly result in deviations of as-built geometry from the CAD data. Hollander et al. [33] reported 30% deviation to predefined diameter of holes (1000 μm) in Ti hollow samples produced by LPBF. Lower deviations (13% (positive) with 1.6% of standard deviation) to predefined hole diameter (500 μm) have been reported by authors [8] in NiTi porous samples produced by micro-direct metal deposition (μDMD) using spot laser diameter of 30 μm . Lower deviation to pre-designed model in μDMD products than LPBF products was attributed to the difference in powder feeding methods. In LPBF, the inner part of a hole is filled by unmolten powder particles that will be removed at the end of the process. Theoretical resolution of LPBF is defined by laser spot size, layer thickness, and thermal characteristics of the powder. However, process parameters have significant effects on practically achievable resolution in micro-scale AM processes [34].

During the LPBF process and when the laser beam forms the border of a hole, a portion of laser input energy is transferred to raw powder particles that are not planned to melt according to the geometry. This transferred energy leads to partial or full melting of excess powder particles and, consequently, results in geometrical deviations with respect to pre-designed geometry. In a recent study [35], deviation to pre-designed model in LPBF of titanium lattice structures was attributed to: (1) the thickening of overhanging horizontal walls, (2) the thinning of vertical walls due to laser parameters and, (3) high energy input from the process. Guo et al. [36] reported melt pool variations in single tracks produced by LPBF process under constant input energy densities. Using X-ray images, they clearly showed that all of the three dimensions of the melt pool (i.e., melt pool length, width and depth) exhibited a trend to increase, while the laser power and laser scan speed within the same input energy density are simultaneously increased. Aiming at minimizing discrepancies in hole diameter between the pre-designed geometry and the as-built NiTi, a new strategy has been employed in this research to implement a complex geometry using μLPBF . As schematically presented in Fig. 9, applying high laser power to form the border of a pre-designed hole may result in a large deviation to predefined hole diameter as presented in Fig. 9c. This phenomenon can be explained by this fact that high laser power leads to increase in melt pool dimensions and consequently partial or full melting of excess powder particles inside the

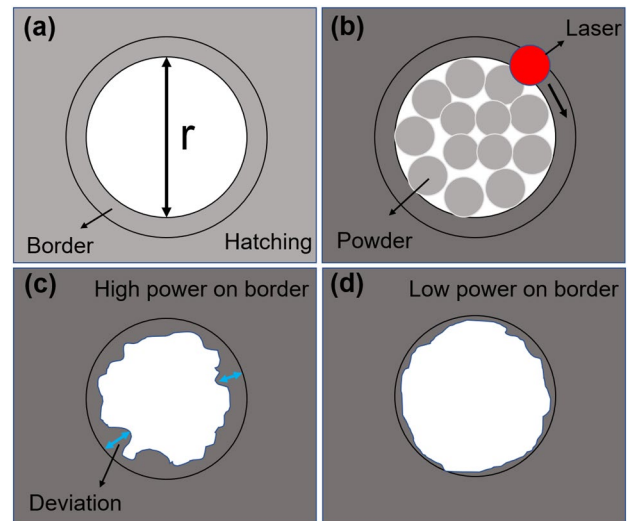


Fig. 9 schematic representation of using different process parameters for border and hatching regions in a hollow sample, **a** top view of a pre-designed model containing border and hatching zones, **b** powder particles inside the hole and moving laser beam on border, **c** high deviation and **d** low deviation of μLPBF processed sample to pre-designed model as a result of using high laser power and low laser power for border, respectively

hole. simultaneous decrease in laser power and scan speed for border under a constant input energy density may reduce this effect as a result of decrease in melt pool dimensions (Fig. 9d). It should be noted that, using different regimes of process parameters leads to different thermal history within the sample. Different thermal histories may lead to the inconsistency in phase composition throughout the sample especially when multiphase materials such as NiTi are being processed. Tan et al. [37] studied the effect of beam compensation and distance between border and hatching area on accuracy of micro-pores in TiNi porous samples produced by LPBF. It should be taken into the account that any differences between hatch distance and border distances may lead to different thermal histories around the micro pores. In the current study, all distances between two adjacent tracks were kept constant at 0.6 mm to ensure consistency in phase composition. As presented in Table 5, three different regimes of μLPBF process parameters in three levels of laser power were developed for fabrication of NiTi dense material. XRD analysis showed that all three regimes led to the single phase B2 austenite microstructure [10]. Therefore, these sets of process parameters can be employed for fabrication of a complex geometry by preserving the phase composition in final product to be mainly B2 austenite.

Lattice structures were designed by replication of diagonal unit cells of two different sizes and were fabricated using μLPBF . Border and hatching zones within a lattice structure are highlighted in Fig. 10a. LP and MP sets of process parameters were used for border and hatching zone,

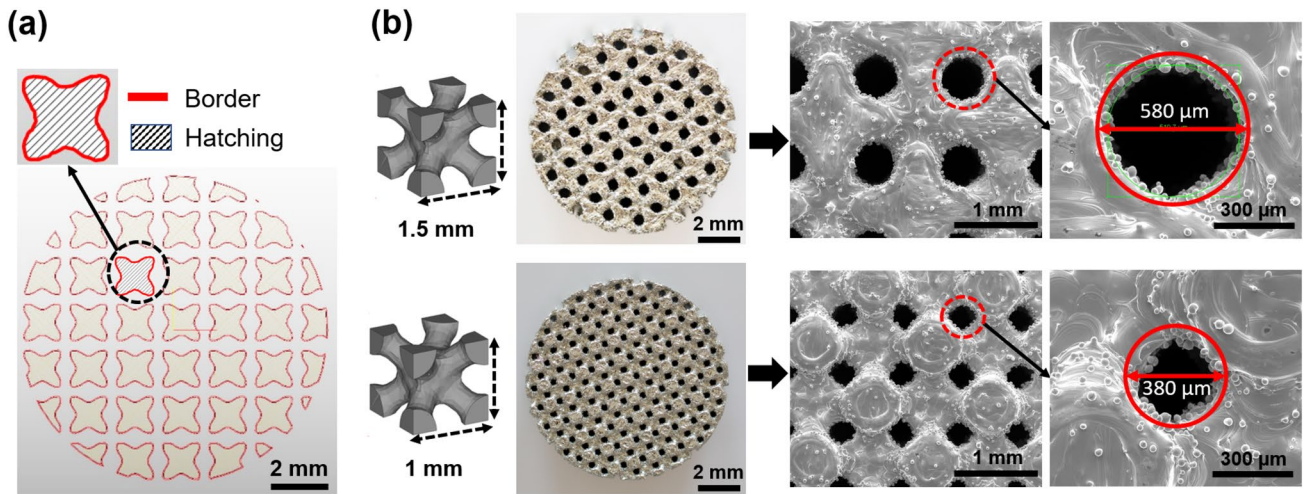


Fig. 10 **a** different μ LPBF process parameters definition for border and hatching regions of lattice structures produced by replication of a diagonal unit cells, **b** top view of NiTi lattice structures produced by

μ LPBF using LP set of parameters for border and MP set of parameters for hatching

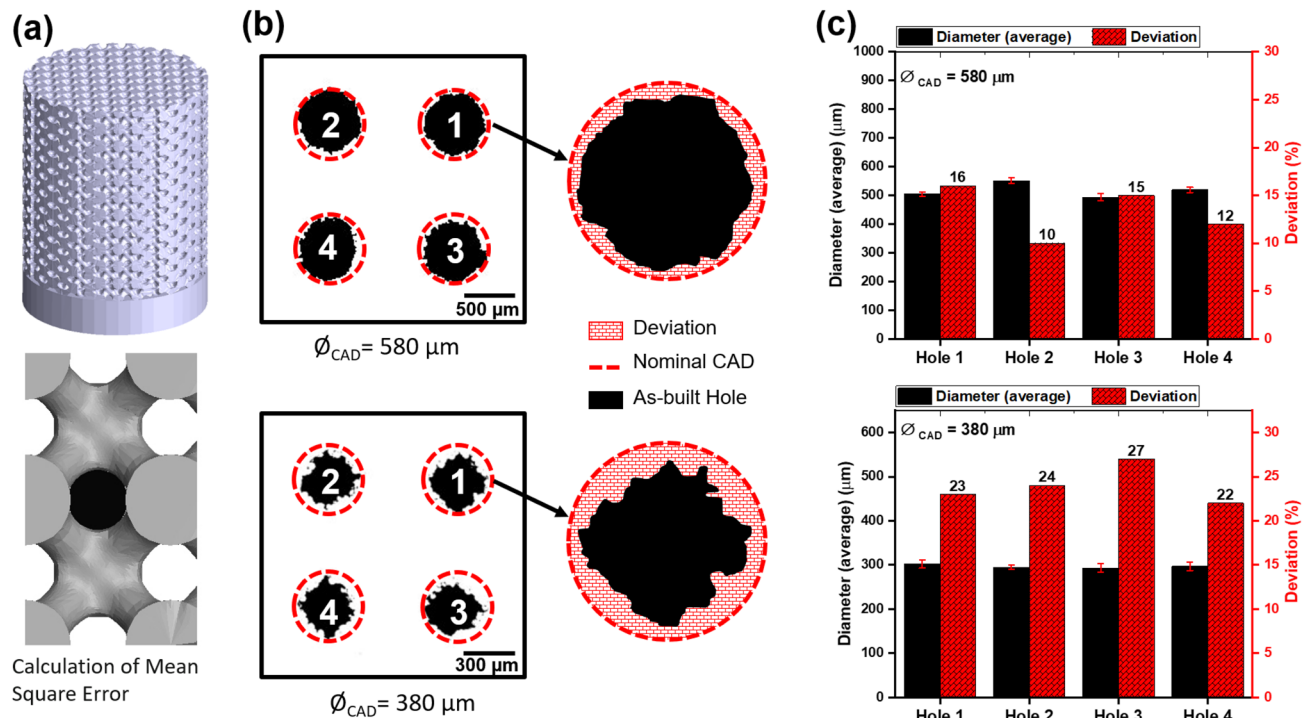


Fig. 11 **a, b** Calculation of deviations in hole diameters in NiTi lattice structures produced by μ LPBF process, **c** average hole diameters and deviations to predesigned values calculated for four individual pores in NiTi lattices samples containing 580 μ m and 380 μ m pores

respectively. The SEM micrographs taken from the top surface of NiTi lattice structures are presented in Fig. 10b for both lattice structures containing 380 μ m-diameter and 580 μ m-diameter predesigned pores.

As can be seen in Fig. 10b, combination of LP and MP set of process parameters led to dense, regular, and defect-free

surface. In opposition to results reported for single tracks [37], increasing laser power from 49 W at border to 70 W in hatching area did not significantly affect the sticking of residual particles on the surface. Deviation of as-built pore diameter in respect to predesigned values were measured through least squares fitting of circular elements as

schematically presented in Fig. 11a, b. The discrepancy between the diameter of as built and predesigned pore can be considered to assess geometric accuracy. The deviation of pore diameter in 580 μm -hole sample distributed in the range 10–16% and the average deviation was approximately 13% (positive). For the 380 μm -hole sample, the deviation ranged from 22 to 27% and the average deviation was approximately 24% (positive). Using in-vitro and in-vivo characterizations, Li et al., showed that scaffolds with predesigned pore size of 300–400 μm are more suitable for the adhesion and proliferation of human bone mesenchymal stem cells. They have reported acceptable bone ingrowth and stability for additively manufactured titanium scaffolds [32]. From Fig. 11b, it is evident that as-built pores are generally smaller than predesigned pores. It is noteworthy to mention that the average aspect ratio of as-built pores for samples with 580 μm and 380 μm pore diameters were 1.05 and 1.12, respectively, which confirms lower shape deviation and more roundness of as-built 580 μm pores in respect to 380 μm pores.

4 Conclusions

In this work, micro-laser powder bed fusion (μLPBF) process was employed for fabrication of NiTi dense and lattice materials with micro-features. The effect of process parameters and post heat treatment on phase transformation temperatures of μLPBF -processed $\text{Ni}_{50.8}\text{Ti}_{49.2}$ was investigated using DSC analysis. Selected process parameters were utilized for fabrication of complex lattice structures aiming at increasing the accuracy of the process. The main results are summarized in the following points.

- Using small spot laser diameter of 30 μm to develop LPBF for microfabrication raised the need for attaining optimum μLPBF process parameters. Input energy density below 50 J/mm^3 resulted in relative density above 99% in $\text{Ni}_{50.8}\text{Ti}_{49.2}$ samples using different levels of laser power (LP: 49 W, MP: 70 W).
- DSC analysis revealed that μLPBF processing of $\text{Ni}_{50.8}\text{Ti}_{49.2}$ using both LP and MP process parameters led to martensite start temperature fairly below the room temperature and consequently austenitic microstructure at room temperature. Age hardening heat treatment resulted in higher TTs due to the formation of Ni-rich precipitates.
- A viable technique was employed to increase the precision of LPBF process and to reduce the deviation of NiTi lattice structures to predefined models. In this approach, different sets of process parameters were used to implement border and hatching area in order to reduce the partially melted powder particles preserving the appropriate phase composition within the printed samples.

- Dimensional accuracy of μLPBF processed NiTi parts with respect to nominal CAD models was quantitatively evaluated using SEM and image analysis. In particular, the obtained deviations values for lattice containing holes with 580 μm nominal diameter and lattice containing hole with 380 μm nominal diameter were 13% and 24%, respectively. Moreover, the deviations between the as-built and nominal parts were found to be mainly positive. This means that the as-built holes are smaller than the predefined values.

References

1. Buehler WJ, Gilfrich JV, Wiley RC (1963) Effect of low-temperature phase changes on the mechanical properties of alloys near composition TiNi. *J Appl Phys* 34:1475
2. Haberland C et al (2014) On the development of high quality NiTi shape memory and pseudoelastic parts by additive manufacturing. *Smart Mater Struct* 23:104002
3. Elahinia M et al (2016) Fabrication of NiTi through additive manufacturing: a review. *Prog Mater Sci* 83:630–663
4. Dadbakhsh S et al (2016) Laser additive manufacturing of bulk and porous shape-memory NiTi alloys: From processes to potential biomedical applications. *MRS Bull* 41:765
5. Jani JM, Leary M, Subic A, Gibson MA (2014) A review of shape memory alloy research, applications and opportunities. *Mater Des* 56:1078–1113
6. Elahinia MH et al (2012) Manufacturing and processing of NiTi implants: a review. *Prog Mater Sci* 57:911–946
7. Haberland C et al (2013) Additive Manufacturing of Shape Memory Devices and Pseudoelastic Components. *Proc ASME Conf Smart Mater Adapt Struct Intel Syst* 1:V001T01A005
8. Khademzadeh S et al (2018) Precision additive manufacturing of NiTi parts using micro direct metal deposition. *Int J Adv Man Tech* 96:3729–3736
9. Bormann T et al (2014) Microstructure of selective laser melted nickel–titanium. *Mater Charact* 94:189–202
10. Khademzadeh S et al (2020) Quality enhancement of microstructure and surface topography of NiTi parts produced by laser powder bed fusion. *CIRP J M Sci Tech* 31:575
11. Smith G (2012) Chapter 10—multiple regression. In: Smith G (ed) *Essential statistics, regression, and econometrics*. Academic Press, New York, p 297
12. Bai S et al (2019) The effects of selective laser melting process parameters on relative density of the AlSi10Mg parts and suitable procedures of the Archimedes method. *Appl Sci* 9:583
13. Steen W (2010) *Laser material processing*. Springer-Verlag, London
14. Dadbakhsh S et al (2014) Texture and anisotropy in selective laser melting of NiTi alloy. *Adv Eng Mater* 16:1140
15. Saedi S et al (2017) Texture, aging, and superelasticity of selective laser melting fabricated Ni-rich NiTi alloys. *Mater Sci Eng A* 686:1
16. Shishkovsky I et al (2012) Direct Selective Laser Melting of Nitinol Powder. *Phys Proc* 39:447
17. Morgan N (2004) Medical shape memory alloy applications—the market and its products. *Mater Sci Eng A* 2(378):16

18. ShayestehMoghaddam N et al (2019) Achieving superelasticity in additively manufactured NiTi in compression without post-process heat treatment. *Sci Rep* 9:41
19. Guan K et al (2013) Effects of processing parameters on tensile properties of selective laser melted 304 stainless steel. *Mater Design* 50:581
20. Ma J et al (2017) Spatial control of functional response in 4D-printed active metallic structures. *Sci Rep* 7:46707
21. Faulkner MG et al (2000) Experimental determination of thermal and electrical properties of Ni–Ti shape memory wires. *Smart Mater Struct* 9:632
22. Tanzi MC et al (2019) Chapter 4—biomaterials and applications, foundations of biomaterials engineering. Academic Press, New York, p 199 (ISBN 9780081010341)
23. Abbasi-Chianeh V et al (2011) Influence of applying external stress during aging on martensitic transformation and the superelastic behavior of a Ni-rich NiTi alloy. *Mater Sci Eng A* 528:5060
24. Prokofiev EA et al (2010) Suppression of Ni₄Ti₃ precipitation by grain size refinement in Ni-rich NiTi shape memory alloys. *Adv Eng Mater* 12:747
25. Abbasi-Chianeh V et al (2013) The effect of post-deformation aging on superelastic properties of Ni50.9Ti thin wires attaining micro and nano-substructure. *J Alloys Comp* 563:44
26. Allafi JK et al (2002) The mechanism of multistage martensitic transformations in aged Ni-rich NiTi shape memory alloys. *Acta Mater* 50:793
27. Eggeler G et al (2005) On the effect of aging on martensitic transformations in Ni-rich NiTi shape memory alloy. *Smart Mater Struct* 14(5):186
28. Otsuka K (2005) Physical Metallurgy of Ti-Ni-Based Shape Memory Alloys. *Prog Mater Sci* 50(5):511
29. Xue L et al (2021) Controlling martensitic transformation characteristics in defect-free NiTi shape memory alloys fabricated using laser powder bed fusion and a process optimization framework. *Acta Mater* 215:117017
30. Khademzadeh S et al (2018) Textural Evolution During Micro Direct Metal Deposition of NiTi Alloy. *Met Mater Int* 24(4):869–876
31. Saedi S et al (2016) The influence of heat treatment on the thermomechanical response of Ni-rich NiTi alloys manufactured by selective laser melting. *J Alloys Comp* 677:204
32. Li G et al (2016) In vitro and in vivo study of additive manufactured porous Ti6Al4V scaffolds for repairing bone defects. *Sci Rep* 6:34072
33. Hollander DA et al (2006) Structural, mechanical and in vitro characterization of individually structured Ti–6Al–4V produced by direct laser forming. *Biomaterials* 27:955
34. Behera D et al (2021) Current Challenges and Potential Directions towards Precision Microscale Additive Manufacturing - Part IV: Future Perspectives. *Precision Eng* 68:197–205
35. Vilardell AM et al (2021) Mechanical behavior of in-situ alloyed Ti6Al4V(ELI)-3 at.% Cu lattice structures manufactured by laser powder bed fusion and designed for implant applications. *J Mech Behav Biomed Mater* 113:104–130
36. Guo Q et al (2019) In-situ characterization and quantification of melt pool variation under constant input energy density in laser powder bed fusion additive manufacturing process. *Addit Manuf* 28:600
37. Tan C et al (2019) Laser powder bed fusion of Ti-rich TiNi lattice structures: process optimisation, geometrical integrity, and phase transformations. *Int J Mach Tool Manu* 141:19–29